Journal Pre-proofs

The role of defects association in structural and transport properties of the $Ce_{1-x}(Nd_{0.74}Tm_{0.26})_xO_{2-x/2}$ system

Cristina Artini, Sabrina Presto, Massimo Viviani, Sara Massardo, Maria Maddalena Carnasciali, Lara Gigli, Marcella Pani

PII: S2095-4956(20)30788-9
DOI: https://doi.org/10.1016/j.jechem.2020.11.030
Reference: JECHEM 1706

To appear in: *Journal of Energy Chemistry*

Received Date: 17 August 2020
Revised Date: 26 November 2020
Accepted Date: 27 November 2020

Please cite this article as: C. Artini, S. Presto, M. Viviani, S. Massardo, M.M. Carnasciali, L. Gigli, M. Pani, The role of defects association in structural and transport properties of the $Ce_{1-x}(Nd_{0.74}Tm_{0.26})_xO_{2-x/2}$ system, *Journal of Energy Chemistry* (2020), doi: https://doi.org/10.1016/j.jechem.2020.11.030

The role of defects association in structural and transport properties of the $Ce_{1-x}(Nd_{0.74}Tm_{0.26})_xO_{2-x/2}$ system

Cristina Artini[a, b, *], Sabrina Presto[c], Massimo Viviani[c], Sara Massardo[a], Maria Maddalena Carnasciali[a,d], Lara Gigli[e], Marcella Pani[a, f]

[a] *DCCI, Department of Chemistry and Industrial Chemistry, University of Genova, Via Dodecaneso 31, 16146 Genova, Italy*
[b] *Institute of Condensed Matter Chemistry and Technologies for Energy, National Research Council, CNR-ICMATE, Via De Marini 6, 16149 Genova, Italy*
[c] *Institute of Condensed Matter Chemistry and Technologies for Energy, National Research Council, CNR-ICMATE, c/o DICCA-UNIGE, Via all'Opera Pia 15, 16145 Genova , Italy*
[d] *INSTM, Genova Research Unit, Via Dodecaneso 31, 16146 Genova, Italy*
[e] *Elettra - Sincrotrone Trieste S.C.p.A., ss 14, km 163.5, 34149 Basovizza, Trieste, Italy*
[f] *CNR-SPIN Genova, Corso Perrone 24, 16152 Genova, Italy*

* Corresponding author.
E-mail address: artini@chimica.unige.it (C. Artini)

ABSTRACT

An experimental investigation of the crystallographic, Raman and transport properties of the $Ce_{1-x}(Nd_{0.74}Tm_{0.26})_xO_{2-x/2}$ ($0.1 \leq x \leq 0.6$) doped ceria system was performed with the aim of setting out correlations between structural features and ionic conductivity of the material. The chosen composition ensures that the average size of the Nd^{3+} and Tm^{3+} doping ions coincides with the one of Sm^{3+}; even so, the studied system presents larger cell parameters and a wider compositional extent of the CeO_2-based solid solution than Sm-doped ceria. Moreover, the occurrence of two different activation energies to ionic conduction below and above ~750 K determines the existence of two distinct conduction regimes. The described experimental results agree with the formation below the threshold temperature of $1V_O^{\bullet\bullet}2Tm'_{Ce}$ trimers, which promote the incorporation of Nd'_{Ce} isolated defects into the CeO_2-based solid solution. In the high temperature range the dissociation

of trimers induces the appearance of a lower activation energy; the extrapolation of its value at infinite dilution provides a result in good accordance with the expected binding energy of $1V_O^{\bullet\bullet}RE'_{Ce}$ dimers, pointing at their stability even in the high temperature conduction regime.

Keywords: Solid oxide fuel cells; RE-doped ceria; High resolution X-ray powder diffraction; Rietveld refinement; μ-Raman spectroscopy; Impedance spectroscopy.

1. Introduction

Co-doping by two or more ions is considered as one of the most effective methods to improve ionic transport in doped ceria, and, consequently, to increase the knowledge of factors ruling transport properties in this class of materials. While structural and transport features associated to single doping are relatively well understood [1,2], multiple doping opens the door to a variety of interconnected phenomena dealing with the enlargement of the CeO_2-based solid solution [3], an unpredicted variation of cell parameters [4] and of free charge carriers [5], as well as a structural disorder increase [6]. Although a huge amount of studies on co-doped ceria are available in the literature, such as the ones on Gd/Y- [7], Gd/Sm- [7,8,9], La/Sm- [10], Sm/Nd- [11], Nd/Gd- [5], Pr/Nd [12], Pr/Gd- [13], Er/Gd- [14], Pr/La- [15], La/Dy- [16], and Nd/Dy- [3] doped CeO_2, the identity of the best composition in terms of ionic conductivity is still controversial. A large number of factors can in fact influence the conduction mechanism, including extrinsic elements like the preparation method and the microstructural features of the sample. In this work for the first time the dominant role of different defects aggregates in ruling the structural and transport properties of multiply doped ceria is highlighted and discussed, thus providing a robust key of interpretation of experimental data, as well as a guide for the choice of the most proper formulations in view of energy production and storage.

Ionic conductivity (σ) is by far the most studied property of rare earth (RE)-doped ceria, since between 773 and 973 K it can be one order of magnitude higher than in yttria-

stabilized zirconia [17]; σ ranging between 0.01 and 0.1 S cm^{-1} at 873 K makes several RE-doped ceria systems potential excellent electrolytes in solid oxide cells working in the intermediate temperature range (IT-SOC) [18]. Ionic conduction occurs by hopping of oxygen ions over vacancies generated by partial substitution of Ce^{4+} with trivalent ions. Doping is most commonly operated by lanthanide ions, due to the Ce^{4+}/RE^{3+} size similarity; within this framework, Sm-, Gd- and Nd-doped ceria are the most relevant systems in terms of ionic transport [2].

The size resemblance of Ce^{4+} and RE^{3+} with coordination number (CN) 8 is essential for preserving the stability of the CeO_2-based solid solution and achieving significant values of ionic conductivity: the fluorite-like (F) atomic arrangement of CeO_2 is in fact the crystallographic environment where ionic transport takes place. This evidence suggests the strict correlation between crystal structure and ionic transport in doped ceria, and the relevance of structural investigation in predicting transport properties; in this respect, x-ray and neutron diffraction, as well as Raman spectroscopy, are the foremost techniques [1,19].

CeO_2 crystallizes in a cubic structure (space group: $Fm\bar{3}m$) [20] containing four formula units per cell; the two atomic positions (0,0,0) and (1/4, 1/4, 1/4) host Ce and O, respectively, and Ce is eight-coordinated to O. At least at low substitution degree, the Ce^{4+} partial replacement gives rise primarily to a solid solution hosting isolated RE'_{Ce} defects and oxygen vacancies, with the latter being free to move at a sufficiently high temperature. The predominance of this phenomenon over other mechanisms of RE^{3+}-vacancy aggregation occurs only up to a certain substitution extent, which is ruled on one hand by the Ce^{4+}/RE^{3+} size closeness, and on the other hand by the binding energy of the RE^{3+}-vacancy clusters [21]. Under these premises, it can be understood why the minimum compositional extent of the F phase is revealed for RE ≡ Gd and Sm [1]. Beyond the limit of the F solid solution, diffraction patterns present superstructure peaks referable to the Ia

$\overline{3}$ space group, which are the signature of the cubic phase (C) typical of the RE^{3+}-vacancy clusters [22], and incidentally of the sesquioxides of the heaviest rare earths (Gd-Lu) [23], where RE is six-coordinated to O. Depending on the Ce^{4+}/RE^{3+} size mismatch, two different scenarios can arise: small lanthanide ions, namely from Lu^{3+} to Tm^{3+}, give rise to a (F + C) two-phase field [24]; the largest ones, on the contrary, stabilize a F/C intermediate (or hybrid, H) phase, consisting in a F-based solid solution with randomly dispersed C microdomains [25,26]. C clusters coherently grow within the F matrix: diffraction peaks common to F and C cannot be separated, irrespective of the instrumental resolution, and the C lattice parameter is exactly doubled with respect to the one of F [27]. The fundamental units building the C-based defect aggregates are $1V_{\mathrm{O}}^{\bullet\bullet}RE'_{\mathrm{Ce}}$ positively charged dimers and $1V_{\mathrm{O}}^{\bullet\bullet}2RE'_{\mathrm{Ce}}$ neutral trimers [28]; even beyond the stability region of the F phase, the presence of isolated RE'_{Ce} defects cannot be *a priori* excluded, but with increasing the RE content, their occurrence becomes progressively less probable in favour of the other two configurations. The stability of dimers and trimers is associated to the maximization of binding energy, which strongly depends on RE^{3+} size, valence state, and local position with respect to the oxygen vacancy [21]; in general, a higher binding energy is calculated for trimers than for dimers, thus pointing at a higher stability of the former [28,29]. Anyway, a dramatic drop of σ is observed in conjunction with the appearance even of tiny amounts of C defect aggregates, due to their blocking effect on the vacancies flow.

Co-doping of ceria has been widely attempted because of the predicted [30] and observed [31] suppressing effect on C clusters, the consequent lowering of activation energy to ionic conduction and, in the end, the enhancement of ionic conductivity [32]. Blocking of oxygen vacancies through the formation of C defects associates is believed to be hindered in multiply doped ceria by the larger configurational entropy existing in such systems with respect to singly doped ones [6]. Co-doping also widens the F region

extent in comparison to a singly doped system with the same doping ion size: an example is offered by $Ce_{1-x}(Nd_{0.63}Dy_{0.37})_xO_{2-x/2}$, having the same RE^{3+} average ionic size of $Ce_{1-x}Sm_xO_{2-x/2}$: the former presents the F/H transition at x~0.5 [4], while the latter at x~0.4 [33].

Considering these premises, the present work was designed as an attempt to improve ionic transport of doped ceria following these three directions: a) doping by a couple of RE^{3+} ions, to extend the F compositional region; b) properly choosing the relative amount of RE^{3+} ions, in order to reproduce the ionic size of Sm^{3+} (CN8), which is an excellent dopant for ceria; c) selecting a couple of doping ions with a large dimensional difference, with the aim to maximize disorder, which is believed to hinder the formation of C clusters, as previously described. As a result, the choice fell on the $Ce_{1-x}(Nd_{0.74}Tm_{0.26})_xO_{2-x/2}$ system, which, relying on the ionic dimensions by Shannon [34] ($r_{Nd3+,CN8}$ = 1.109 Å, $r_{Tm3+,CN8}$ = 0.994 Å), displays an average RE^{3+} ions size of 1.079 Å, namely the one of Sm^{3+} (CN8). The structural, microstructural, Raman and transport properties of the system with x ranging between 0.1 and 0.6 were investigated; correlations between crystallographic features, local structure of C clusters, and ionic conductivity, were established and discussed.

2. Materials and methods

2.1 Synthesis

Six samples belonging to the $Ce_{1-x}(Nd_{0.74}Tm_{0.26})_xO_{2-x/2}$ system with nominal x = 0.1, 0.2, 0.3, 0.4, 0.5 and 0.6, were prepared by coprecipitation of mixed oxalates, as described in [35]. For each composition, proper amounts of Ce (Johnson Matthey ALPHA 99.99% wt.), Nd_2O_3 (Alfa Aesar, 99.99 wt%), and Tm_2O_3 (Mateck, 99.99 wt%) were separately dissolved in HCl (13% vol.); then, the three solutions were mixed. Afterwards, a solution of oxalic acid in excess was added to the mixtures to promote the precipitation of the mixed Ce/Nd/Tm oxalates, which were then filtered, washed, dried for 12 h, and treated

at 1373 K in air for four days to obtain the corresponding mixed oxides with a high crystallinity degree. Specimens were named NdTm10, NdTm20, and so on, according to the nominal (Nd,Tm) atomic percent with respect to the total lanthanide content.

2.2 Scanning electron microscopy – energy-dispersive system (SEM-EDS)

The overall lanthanide content was checked by scanning electron microscopy with field emission gun and energy-dispersive system (FE-SEM-EDS, Zeiss SUPRA 40 VP-30-51 scanning electron microscope, equipped with a high sensitivity 'InLens' secondary electron detector and an EDS microanalysis INCA Suite Version 4.09, Oxford Instruments). Samples were pelletized, graphite-coated and analyzed at a working distance of 15 mm, with acceleration voltage 20 kV. EDS analyses were performed on at least 5 points for each composition.

2.3 Synchrotron x-ray powder diffraction

Diffraction patterns of all the specimens were collected at room temperature at the powder diffraction beamline (MCX) [36] of the Elettra synchrotron radiation facility located in Trieste, Italy, making use of a Huber 4-axes X-ray diffractometer equipped with a fast scintillator detector. Samples were placed in borosilicate capillary tubes (inner diameter: 0.5 mm) and rotated at a speed of 180 rpm. Diffractograms were acquired in the angular range $5° \leq 2\theta \leq 55°$ with step 0.01°, counting time 1 s, and the incident beam energy set at 18 keV (λ = 0.68927 Å). Annealed LaB_6 was used as a standard reference material both to calibrate the incident wavelength, and to account for the instrumental peak broadening. To the latter purpose, the instrumental resolution function, needed to separate instrument- from sample-dependent broadening effects, was determined according to the following expression:

$$\beta^2 = \beta_{\text{tot}}^2 - \beta_{\text{instr}}^2 \quad (1)$$

where β, β_{tot} and β_{instr} are the sample-related, overall, and instrumental broadening, respectively. The peak shape of the standard material was optimized through the Thompson-Cox-Hastings function [37].

Structural models were refined by the Rietveld method using the FullProf suite [38]. Peak profiles were optimized using the Pseudo-Voigt function, while the background was refined by linear interpolation of a set of ~70 points taken from the experimental pattern. The absorption coefficient was accounted for by introducing for each sample a correction factor determined from the Ce/Nd/Tm proportion and the measured packing density of the powder. Atomic displacement parameters B were refined for each Ce/Nd/Tm position; in the H model the same B was attributed to both O atoms and subsequently optimized; the atomic content of Ce, Nd and Tm was fixed to the value provided by EDS and not refined, due to the closeness of the scattering factor of the involved elements. Fig. 1 shows the Rietveld refinement plot of sample NdTm40 as a representative example; all the other refinement plots, as well as CIF files, are reported as Supplementary Information.

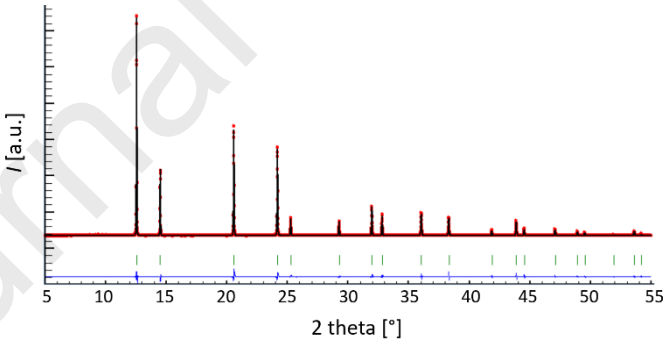

Fig. 1. Rietveld refinement plot of sample NdTm40. The red dotted and the black continuous lines are the experimental and calculated pattern, respectively; the blue line at the bottom is the difference curve. Green vertical bars correspond to the calculated positions of Bragg peaks.

2.4 μ-Raman spectroscopy

Room temperature Raman spectra were collected by a Renishaw System 2000 Raman imaging microscope; analyses were performed within the 1500-100 cm^{-1} range using a 633 nm He–Ne laser on powder samples, as a result of 1 accumulation lasting 10 s. Spectra were acquired with a 50× magnification lens on at least 3 points for each specimen. The laser power was kept at around 4 mW; the wave number has an accuracy of 3 cm^{-1}.

2.4 Impedance spectroscopy

Samples were pelletized by uniaxial pressing and subsequently sintered in air at 1773 K for 1 h. Metallic electrodes were laid on plane surfaces of the sintered bodies by brushing Pt paste (Metalor, Birmingham-UK), followed by curing in air at 1273 K for 10 minutes. For the estimation of ionic conductivity, samples were placed in a Probostat A test rig (NORECS AS, Oslo - Norway). Impedance spectroscopy measurements were carried out by a Frequency Response Analyzer (Iviumstat, IVIUM Technologies b.v., Eindhoven- NL) in the 500-1000 K temperature range under flowing synthetic air (30 Nml/min). For each temperature the resistance (R) was estimated by subtracting the electrodes contribution from impedance spectrum. Ionic conductivity was then calculated by the standard Ohm's law.

3. Results

3.1 Structural and microstructural characterization

EDS analyses highlight a good agreement between nominal and experimental x values. The particles size, roughly ranging between 0.5 and 2 μm, and globally increasing with the doping ion content as already noticed for the $Ce_{1-x}(Nd_{0.63}Dy_{0.37})_xO_{2-x/2}$ system [4], can be appreciated by observing microphotographs taken on NdTm30 and NdTm40 reported as Supplementary Information.

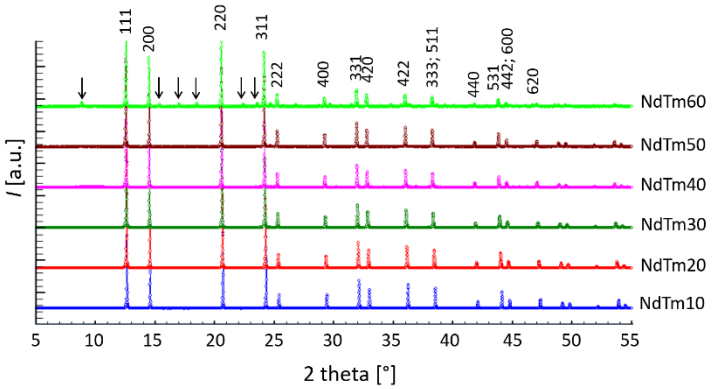

Fig. 2. Stacked diffraction patterns of $Ce_{1-x}(Nd_{0.74}Tm_{0.26})_xO_{2-x/2}$ samples. The occurrence of peaks attributable to phase C are indicated by arrows; Miller indexes of peaks belonging to the F phase are reported too.

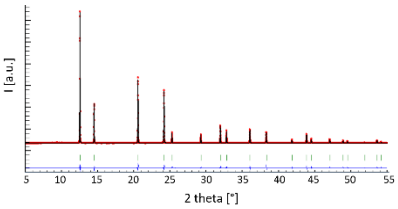

The occurrence of either F or C diffraction peaks drove the choice of the structural model to be refined for each sample. According to Fig. 2, C peaks appear at the nominal x value 0.60, while at lower x only F peaks are recognizable. Moreover, in NdTm60 the coincidence of the peaks common to both structures implies that beyond the F region, the hybrid (H) phase is stable: this evidence, if compared to the occurrence of the (F + C) two-phase field in Tm-doped ceria [24], points at the role of the larger Nd^{3+} ion as stabilizer of H. The F model was then refined up to $x = 0.50$, the H model at $x = 0.60$. The H model can be deemed as a transposition of the F structure into the $Ia\bar{3}$ space group, *i.e.* the one describing the C structure: crystallographic sites fixed by symmetry in $Fm\bar{3}m$ are no more constrained in $Ia\bar{3}$, and atomic coordinates approach the values typical of the C-structured RE_2O_3 with increasing the doping ions content. This is the case of the Ce/RE1 x crystallographic site, which assumes the value ¼ in $Fm\bar{3}m$, while starting from the F/H crossover it regularly moves toward ~0.28; therefore, an abrupt slope change occurs at the transition, as revealed in Gd- [27] and in Sm- [33] doped ceria. Besides, to correctly

describe $Ce_{1-x}RE_xO_{2-x/2}$ mixed oxides according to the H model, an additional position is needed in 16*c* to place oxygen atoms in excess with respect to the RE_2O_3 stoichiometry. Details of both models can be found as Supplementary Information.

The structural properties of the studied system can be in more depth understood if analysed in comparison to the ones of $Ce_{1-x}(Nd_{0.63}Dy_{0.37})_xO_{2-x/2}$ [4] and $Ce_{1-x}Sm_xO_{2-x/2}$ [33], as all of them share the same average size of the doping ion(s). This combined approach suggests the relevance of two main items, namely the size of lattice parameters, and the position of the F/H crossover.

Fig. 3 reveals that lattice parameters of all the series increase with *x*, as expected from the larger size of all the involved doping elements with respect to Ce^{4+} ($r_{Ce4+,CN8}$ = 0.97 Å; $r_{Nd3+,CN8}$ = 1.109 Å; $r_{Dy3+,CN8}$ = 1.027 Å; $r_{Tm3+,CN8}$ = 0.994 Å) [34]. Despite the formation of a solid solution, the increase is not linear, due to the decrease in the oxygen content occurring with increasing *x*, which makes Vegard's law [39] not applicable. This behaviour was already observed in the similar Gd- [27,40] and Lu- [25] doped ceria systems. The comparison among the series highlights the larger size of the cell parameters of doubly-doped with respect to Sm-doped ceria, notwithstanding the nearly identical average size of the doping ion(s); moreover, data of the (Nd,Dy)- and (Nd,Tm)-based systems are nearly superimposable.

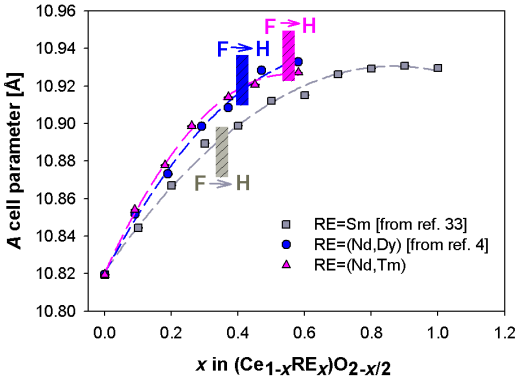

Fig. 3. Refined lattice parameters of (Nd,Dy)- [4], (Nd,Tm)- and Sm- [33] doped ceria *vs.* the doping ion(s) content; cell parameters of F-structured samples are doubled in order

to directly compare them with the ones of H samples. The approximate position of the F/H crossover is indicated for each series. Data are fitted by second order polynomial functions (dashed curves); error bars are hidden by data markers.

The position of the F/H crossover can be localized through several different structural markers: results are not identical, since they reflect the sensitivity of the chosen indicator, but the qualitative outcome, pointing at a larger F region in doubly doped systems, is preserved. According to the appearance of C diffraction peaks, for instance, the compositional width of the F region extends in $Ce_{1-x}(Nd_{0.74}Tm_{0.26})_xO_{2-x/2}$, $Ce_{1-x}(Nd_{0.63}Dy_{0.37})_xO_{2-x/2}$, and $Ce_{1-x}Sm_xO_{2-x/2}$, at least up to x = 0.50, 0.40 [4], and 0.30 [33], respectively. Therefore, even the Nd/RE difference seems to play a role, since the widest F region occurs for the system with the largest size difference. As aforementioned, the F/H crossover can be localized also relying on the Ce/RE1 *x* crystallographic site, namely a more sensitive and accurate parameter with respect to the mere observation of the presence of C diffraction peaks. Following this idea, the diffraction patterns with only F peaks were also treated according to the C model in order to let the cited position vary during refinements. In Fig. 4, the refined values of the Ce/RE1 *x* position are reported *vs.* the dopant content for all the three series. Both doubly doped systems display the expected kink at $x \sim 0.4$, while in Sm-doped ceria the slope change occurs at $x \sim 0.3$, thus confirming the wider extent of the F region in the former systems. Though, even doubly doped series do not behave identically: within the H region, in fact, at each composition the (Nd,Tm)-based system presents the lowest Ce/RE1 *x* values, followed by (Nd,Dy)-, and finally by Sm-doped ceria. This evidence again suggests that also the Nd/RE size difference plays a role: the larger the difference, the closer the Ce/RE1 *x* position to 0.25, namely to the value typical of the F structure; for RE ≡ Sm, on the contrary, the Ce/RE1 *x* position is the closest to 0.28, namely to the value typical of C-structured RE_2O_3 oxides. This

evidence suggests the sensitivity of the F/H transition not only to the mean doping ion size, but, in case of multiple doping, also to the size difference between doping ions, underlining that the crossover position is finely tuned through structural details not limited to the cited slope change.

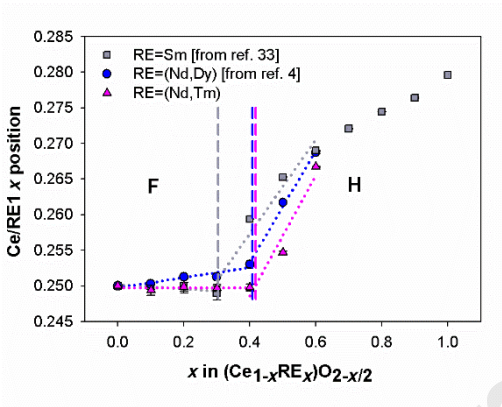

Fig. 4. Refined Ce/RE1 x position values of the (Nd,Dy)- [4], (Nd,Tm)- and Sm- [33] doped systems *vs.* the doping ion(s) content. Error bars are sometimes hidden by data markers. Dotted lines are regression lines fitting data, while vertical dashed lines approximately indicate the position of the F/H crossover.

The microstructural analysis of diffraction data, aimed at unveiling the possible effect of the doping ions size on microstrain and/or on the diffraction domains size from the integral breadth (β) of peaks, provides a further hint to the localization of the F/H crossover. Among the possible approaches, the Williamson-Hall (W-H) method [41] was chosen for its simplicity, which makes it ideal for an initial screening of a material's microstructural features. According to this method, the quantity $\frac{\beta\cos\theta}{\lambda}$ can be obtained from the following expression:

$$\frac{\beta\cos\theta}{\lambda} = \frac{0.9}{D} + 2\varepsilon d^* \qquad (2)$$

with d^* the distance in the reciprocal space between planes of the considered family. The plot of $\frac{\beta\cos\theta}{\lambda}$ *vs.* d^* provides a straight line if peak broadening is isotropic, *i.e.* if

microstrain is independent of the crystal lattice direction; the upper microstrain limit (ε) and the apparent diffraction domains size (D) are obtained from slope and intercept, respectively.

Fig. 5 represents the refined values of maximum ‰ microstrain *vs.* the doping ions content for $Ce_{1-x}(Nd_{0.74}Tm_{0.26})_xO_{2-x/2}$. The rise up to x = 0.3 is fully compatible with the strain produced by the progressive incorporation of the rare earths mixture into the CeO_2-based solid solution, inducing both positive and negative local deviations of d-spacings from the average value. It is noteworthy that at each composition the extent of the 2ϑ dispersion giving rise to peak broadening (and hence to the observed microstrain) is comparable to the 2ϑ peak shift with respect to the peak positions of CeO_2. This result means that the stress induced by the insertion of larger foreign RE atoms promotes at the average scale the observed cell parameter increase, and at the local scale a wide distribution of cell sizes, therefore a high disorder degree. At x > 0.3 the formation of C defect clusters subtracts a certain amount of doping ions from the F solid solution, thus causing a sudden strain release. The microstrain increase observable from x = 0.5, on the contrary, can be justified by two different reasons. On one hand, provided that at such high x values doping ions mainly enter C microdomains, it can be caused by an increase in the doping ions content even of the F phase. On the other hand, it can be related to the entrance of small amounts of Ce^{4+} into C microdomains. This hypothesis is supported in Sm-doped ceria by the sudden increase of the Raman shift of the signal at ~370 cm^{-1}, related to the C phase, with decreasing the RE^{3+} amount from 0.8 to 0.7 [33]. This evidence can be attributed to the presence of a little amount of the smaller Ce^{4+} in place of the larger Sm^{3+} within C microdomains. Therefore, based on the microstrain outcome, the F/H transition is thus located within the 0.3-0.4 x range, again highlighting the strong dependence of the crossover position on the structural parameter taken as a marker.

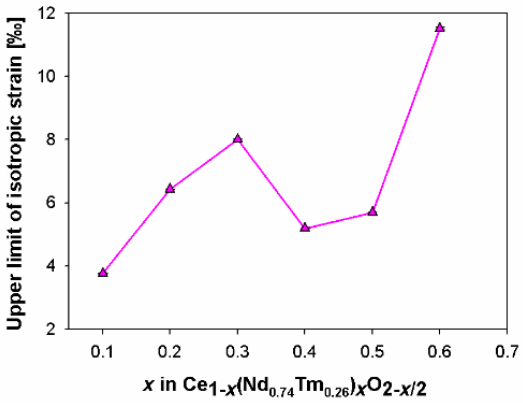

Fig. 5. Plot of the upper ‰ limit of isotropic microstrain *vs.* x in the $Ce_{1-x}(Nd_{0.74}Tm_{0.26})_xO_{2-x/2}$ system.

3.2 Raman characterization

In Fig. 6 the normalized Raman spectra of $Ce_{1-x}(Nd_{0.74}Tm_{0.26})_xO_{2-x/2}$ samples and CeO_2 [33] are collected. The signal at ~465 cm^{-1}, attributed to the F_{2g} symmetric vibration mode of the Ce-O bond in eightfold coordination [42,43], occurs at each composition while becoming broader and less intense with increasing the doping ions amount. At the same time, vacancies-related Raman bands due to the introduction of the trivalent doping ions, appear starting from NdTm20 at ~190 cm^{-1}, ~250 cm^{-1}, ~540 cm^{-1} and ~600 cm^{-1}; besides, the last-mentioned signal tends to disappear with increasing x, being hidden by the one at ~540 cm^{-1}. The clearly recognizable signal occurring at x = 0.40 close to 370 cm^{-1}, which sharpens and grows with increasing x, is ascribed to an $(A_g + F_g)$ RE-O symmetrical stretching mode with RE in six-fold coordination [44], thus suggesting the existence of C-structured defect associates at a composition not giving rise to any C peak in diffraction patterns. Similarly, in Sm-doped ceria the signal at ~370 cm^{-1} occurs at x = 0.30, while C diffraction peaks are visible starting from x = 0.40 [33], thus confirming the higher sensitivity of Raman spectroscopy toward the detection of C-based defect clusters.

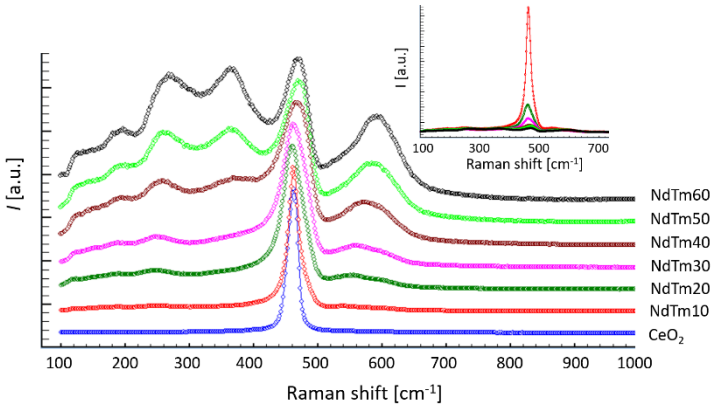

Fig. 6. Normalized Raman spectra of samples belonging to the $Ce_{1-x}(Nd_{0.74}Tm_{0.26})_xO_{2-x/2}$ series. Inset: enlarged view of raw spectra.

The drastic intensity decrease of all Raman signals with increasing the doping ions content, observable in the inset to Fig. 6, agrees with the reduction of the RE polarizability associated to the progressive substitution of Ce^{4+} with CN 8 (in the F phase) by the smaller RE^{3+} ions with CN 6 (in the C phase).

The general trend of the signal at ~465 cm^{-1} *vs.* the RE doping ions content is common to many doped ceria systems, such as the Sm- [33], Gd- [33] and Lu- [25] based ones, and it consists in an initial Raman shift decrease, due to the introduction into the F lattice of a larger ion (or ions mixture) in place of Ce^{4+}, which reduces the energy needed to excite the vibration along the Ce/RE-O bond. At higher dopant content, the Raman shift starts increasing, due to the growth within F of the oxygen vacancies amount, responsible for lattice shrinkage [43–47]. The x value corresponding to the minimum represents the crossover between the compositional range where the ionic size is the dominant contribution to Raman shift, and the one where vacancies prevail; in this respect, it can be deemed as a further indicator of the F/H transition. Once more, the comparative approach with the behavior of Sm-doped ceria [33] aids in understanding the effect of the (Nd,Tm) substitution at the Ce^{4+} site.

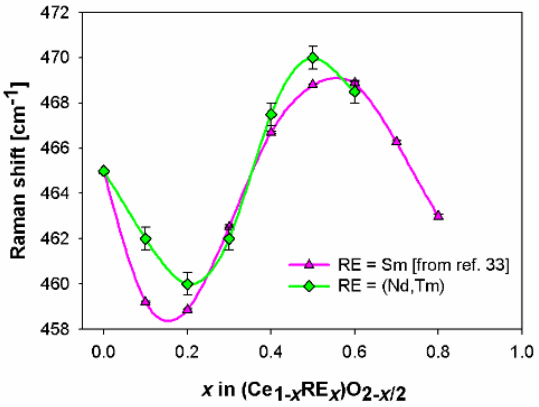

Fig. 7. Raman shifts of the signal at ~465 cm^{-1} for (Nd,Tm)- and Sm- [33] doped ceria *vs.* composition. Data are fitted by splines.

In Fig. 7 the Raman shifts of the band at ~465 cm^{-1} are reported *vs. x* for both systems: Sm- and (Nd,Tm)-doped ceria present similar values, as expected from isostructural systems characterized by very close ionic dimensions; discrepancies can be observed at low dopant content revealing the occurrence of the minimum at x ~0.15 for Sm-, and ~0.20 for (Nd,Tm)-doped ceria, and again confirming the wider extent of the F phase in the latter system. Finally, beyond x ~0.5 the Raman shift decreases, marking a further boundary observable at the same x value also in the trend of several structural parameters of Y- [48], Sm- [33] and Gd-doped ceria [33] (see for example data of Sm-doped ceria in Fig. 4); it shows to be independent of the dopant chemical nature, thus pleading for a topological origin of the phenomenon. This interpretation is confirmed recalling that 0.5 is the percolation threshold of a randomly distributed second phase in a square lattice [49], thus allowing to hypothesize that beyond this limit domains of the C phase are connected throughout the whole atomic arrangement. Based on these premises, the Raman shift decrease occurring at $x \geq 0.5$ is ascribable to the progressive incorporation into C domains of defects subtracted from the F phase.

Moving to vacancies-related signals, a substantial coincidence of Raman shifts of both systems can be observed in the band at ~540 cm^{-1} (see Fig. 8), as expected from a signal caused by the interaction between the vacancy and the 6 next-nearest neighbor O atoms, thus not involving doping ions [50].

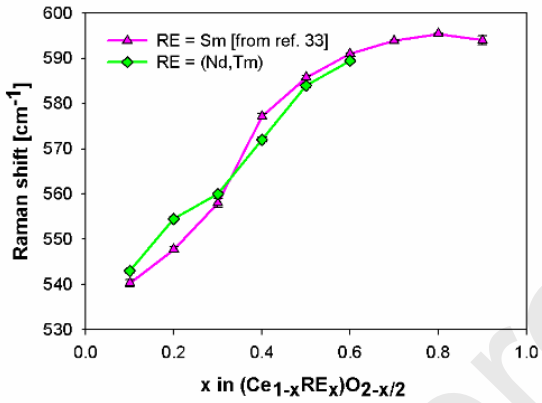

Fig. 8. Raman shifts of the signal at ~540 cm^{-1} for (Nd,Tm)- and Sm- [33] doped ceria *vs.* composition. Data are connected by broken lines.

Raman shifts of the signal at ~370 cm^{-1}, namely the signature of the C phase, on the contrary, are quite different in the two systems, as evident from Fig. 9. Data of (Nd,Tm)-doped ceria are in fact higher and tend to align to the values of Sm-doped ceria from x = 0.6. The reasons for this behavior will be analyzed in more detail in the discussion.

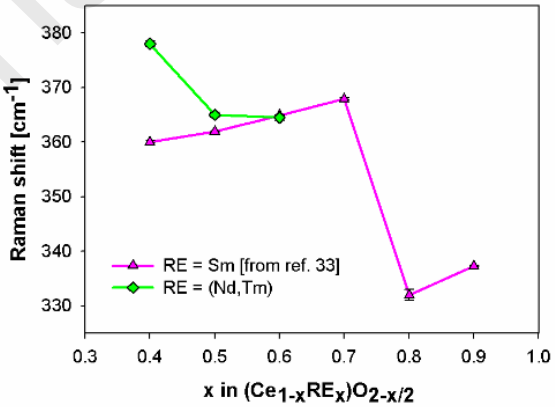

Fig. 9. Raman shifts of the signal at ~370 cm^{-1} for (Nd,Tm)- and Sm- [33] doped ceria *vs.* composition. Data are connected by broken lines.

3.3 Ionic conductivity measurements

The dependence of ionic conductivity (σ) data on x is shown in Fig. 10. The maximum σ is observed at each temperature at x ~0.30: considering that in Sm-doped ceria it is found between x = 0.19 and x = 0.24 [51], the wider extent of the F region in the doubly doped system is again confirmed. Similarly to other doped ceria systems [39,52,53], even the present one displays the maximum of conductivity followed by a drop well within the compositional limits of the F region revealed by x-ray diffraction: this result corroborates the presence of C-based defect aggregates even at very low dopant amount, as also confirmed by Raman spectroscopy.

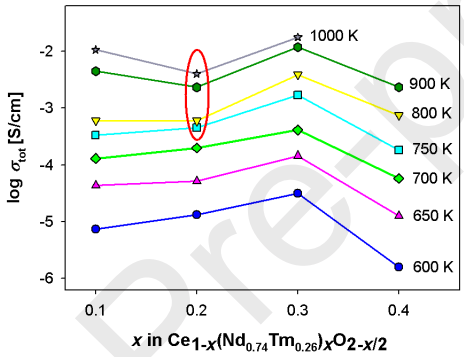

Fig. 10. Dependence of $log(\sigma)$ on x. Experimental data are connected by broken lines. Data collected at temperature as high as 750 K of NdTm20 are circled.

σ data were fitted to the Arrhenius equation

$$\sigma T = Aexp\left(-\frac{E_a}{RT}\right) \quad (3)$$

where A is the pre-exponential factor, E_a is the activation energy to ionic conductivity, and R the gas constant; results are shown in Fig. 11. While data of NdTm10 can be conveniently fitted by a single regression line, the other compositions present two different slopes, with the steeper one at lower temperature; indeed, the existence even in NdTm10 of two different slopes, yet indistinguishable due to the insufficient sensitivity of the experimental set-up, cannot be excluded. The occurrence of a kink in the Arrhenius

plot implies the existence of two different activation energies (in particular the higher one at lower temperature), which are commonly attributed to the presence of vacancies mostly trapped in C domains at low temperature, and mostly free at high temperature. When revealed, the high/low temperature E_a difference is referred to as "apparent association enthalpy" [54].

The transition between the two regimes can be localized at the slope change of the Arrhenius plot; crossover temperatures are reported *vs.* x in the inset to Fig. 11. As a matter of fact, ~750 K is generally reported as the crossover temperature irrespective of the doping ion [2]; the trend observed in the present work can be attributed to the increasing binding energy associated to the growing size of C defect clusters [21,22], which makes progressively more difficult to force vacancies out of C clusters.

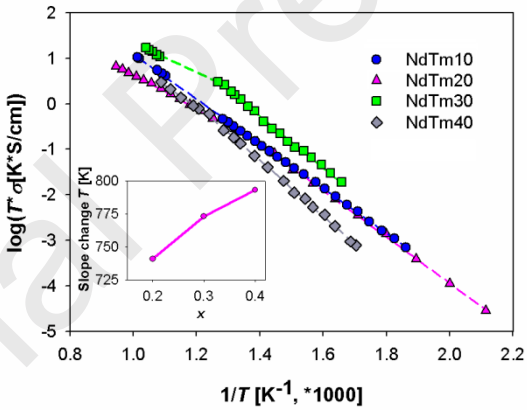

Fig. 11. Arrhenius plots of ionic conductivity of the $Ce_{1-x}(Nd_{0.74}Tm_{0.26})_xO_{2-x/2}$ system. Dashed lines are regression lines fitting experimental data. Inset: temperature of slope change *vs.* the doping ions content.

Calculated activation energies are reported in Fig. 12 *vs.* x. Low temperature values follow a regularly increasing trend, while high temperature ones present a minimum at x ~0.3, in agreement with the occurrence of maximum σ at this composition.

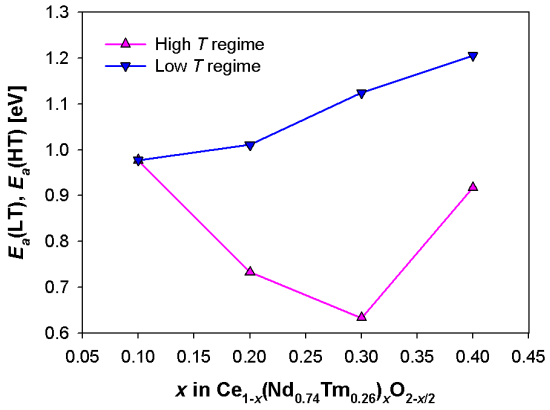

Fig. 12. Activation energies to ionic conductivity for the $Ce_{1-x}(Nd_{0.74}Tm_{0.26})_xO_{2-x/2}$ system *vs.* x.

4. Discussion

The key to a coherent interpretation of the described data, is provided by the nature and stability of C defect aggregates as a function of temperature and doping ions size.

Atomistic simulations show that with decreasing the RE^{3+} radius the binding energy of $1V_O^{\bullet\bullet}2RE'_{Ce}$ trimers increases if the doping ion is in the nearest-neighbour (NN) location with respect to the vacancy, while it slightly decreases if it is located in the next-nearest neighbour (NNN) position [21,55]. As a consequence, a NN/NNN crossover occurs close to the ionic size around 1.12 Å, and a minimum of binding energy can be found either between RE ≡ Pr^{3+} and Sm^{3+} [21,56], or near RE ≡ Gd^{3+} [28]; these predictions are in excellent agreement with σ experimental results, which set the maximum at RE ≡ Gd^{3+} and Sm^{3+}. Anyway, whatever the position of RE with respect to the vacancy, the binding energy is always higher for $1V_O^{\bullet\bullet}2Tm'_{Ce}$ aggregates than for $1V_O^{\bullet\bullet}2Nd'_{Ce}$ ones, which leads to hypothesize that in (Nd,Tm)-doped ceria C defect clusters are more stable and more easily formed by Tm than by Nd.

Relying on these considerations, the larger cell parameter observed in (Nd,Tm)- than in Sm-doped ceria finds its explanation considering that within the F region, C clusters

are mainly $1V_O^{\bullet\bullet}2Tm'_{Ce}$defect associates; as a consequence, RE^{3+} ions dispersed within the F matrix essentially consist in Nd^{3+}, which, being larger than Sm^{3+}, causes the observed cell size difference. The stability of $1V_O^{\bullet\bullet}2Tm'_{Ce}$ trimers also originates the enlargement of the F phase compositional span: it is in fact documented in the literature that the F region extent roughly linearly increases with increasing the ionic size for RE^{3+} larger than Gd [1]; in particular, in $Ce_{1-x}Nd_xO_{2-x/2}$ it extends up to x = 0.4-0.5 [43,57–59]. Several mechanisms can be invoked to interpret this behaviour, but the main reason seems to be two-fold: on one hand, the relatively low binding energy of both $1V_O^{\bullet\bullet}Nd'_{Ce}$dimers and 1 $V_O^{\bullet\bullet}2Nd'_{Ce}$ trimers with respect to the same Sm-based configurations, which favours the stability of the F phase [21]; on the other hand, a more general issue, regarding the already mentioned larger configurational entropy of doubly- with respect to singly-doped ceria, in the present system also testified by the observed increase in microstrain, which tends to suppress C clusters [6]. All these considerations are reinforced by comparing results of the present and the $Ce_{1-x}(Nd_{0.63}Dy_{0.37})_xO_{2-x/2}$ [4] system: the slightly smaller cell parameter, as well as the reduced F compositional range of the latter, can be ascribed to the smaller binding energy of $1V_O^{\bullet\bullet}2Dy'_{Ce}$ associates with respect to $1V_O^{\bullet\bullet}2Tm'_{Ce}$ ones [21], which favours the occurrence of a higher concentration of isolated Dy'_{Ce} than Tm'_{Ce} (notwithstanding the large majority of isolated Nd'_{Ce} defects in both systems).

The prevailing formation of $1V_O^{\bullet\bullet}2Tm'_{Ce}$ over $1V_O^{\bullet\bullet}2Nd'_{Ce}$ is also confirmed by the analysis of the Raman shift of the signal at ~370 cm^{-1}, distinctive of the C phase (see Fig. 9). The higher Raman shift for $Ce_{1-x}(Nd_{0.74}Tm_{0.26})_xO_{2-x/2}$ than for $Ce_{1-x}Sm_xO_{2-x/2}$ at x = 0.4 and 0.5 points in fact at the preferential creation of Tm_2O_3 C clusters with respect to Nd_2O_3 ones, being the former characterized by a remarkably smaller cell size with respect to Sm_2O_3 C domains ($r_{Sm3+,CN6}$ = 0.958 Å, $r_{Tm3+,CN6}$ = 0.880 Å, $r_{Nd3+,CN6}$ = 0.983 Å) [34]. Moreover, in view of the shrinking effect of vacancies on the F lattice, the generally

higher Raman shift of the signal at ~465 cm^{-1} occurring for $Ce_{1-x}(Nd_{0.74}Tm_{0.26})_xO_{2-x/2}$ than for $Ce_{1-x}Sm_xO_{2-x/2}$ (see Fig. 7), points at a higher content of free vacancies in the former. This conclusion is consistent with the preferred entrance into F, as randomly dispersed Nd'_{Ce} defects, of Nd^{3+} ions, namely the quantitatively prevailing RE^{3+} species.

The stability of C aggregates is focal even for the comprehension of ionic transport in the studied system. The occurrence of the two-fold activation energy can be also indirectly revealed in the trend of $\log(\sigma)$ *vs.* x by the presence of a minimum in σ at x ~0.20 at temperatures as high as 750 K (see circled data in Fig. 10). This evidence, also observed in (Gd,Sm)-doped ceria [6], can be better understood going back to Fig. 11: the occurrence of the very same σ in the low temperature range for both NdTm20 and NdTm10, coupled to the lower E_a for the former at high temperature, gives rise to the described drop in conductivity.

It is well established that activation energy to ionic conduction is formed of two additive terms, namely the migration enthalpy (H_m) and the association enthalpy (H_a), being the former the energy needed by free vacancies to move through the lattice, and the latter the energy difference between isolated defects and defect clusters, *i.e.* the energy necessary to release vacancies from defect clusters [53]. According to several studies, H_m is considered as independent of the RE identity, and roughly equal to 0.6-0.7 eV [60–62]. The evaluation of H_a, on the contrary, cannot disregard the existence of both dimers and trimers, with trimers being characterized by a higher binding energy, as previously discussed. Therefore, at low temperature, E_a can be expressed as the sum of three terms:

$$E_a(LT) = H_m + H'_a + H''_a \quad (4)$$

with H'_a the association enthalpy of dimers and H''_a the association enthalpy of trimers. Increasing temperature over the threshold at ~750 K can be hypothesized as causing the disappearance of trimers, due to their low configurational entropy [63]; in the light of

these assumptions, the association enthalpy of trimers (H''_a) can be interpreted as the apparent association enthalpy, according to the following expression:

$$H''_a = E_a(LT) - E_a(HT) \quad (5)$$

while H'_a assumes the following value:

$$H'_a = E_a(HT) - H_m \quad (6)$$

Using experimental $E_a(LT)$ and $E_a(HT)$, and the aforementioned H_m constant value (0.6 eV), H'_a and H''_a were calculated and reported *vs. x* in Fig. 13. It can be observed that H''_a, namely the association enthalpy of $1V_O^{\bullet\bullet}2RE'_{Ce}$ trimers, increases up to nominal x = 0.30 and subsequently decreases. This result is in very good agreement with the predicted effect of strain on oxygen diffusivity through doped and co-doped ceria [63], which is expected to induce a significant decrease of the oxygen diffusion coefficient, directly reflecting in an increase of the C defects aggregates association enthalpy.

Conversely, the trend of H'_a significantly decreases up to x ~0.30, namely up to the RE^{3+} concentration corresponding to the maximum σ. As previously briefly outlined, H'_a essentially consists of the C dimers association enthalpy, since the low configurational entropy of C trimers favours their disappearance in the high temperature range.

Moreover, at variance with H''_a, H'_a depends on $E_a(HT)$ and is not related to $E_a(LT)$. Its behaviour can be thus studied taking into consideration the exhaustive treatment of E_a (HT) contained in the work by Wang *et al.* [61], who analysed the behaviour of Y-doped ceria in the dilute range. According to this study, H'_a is properly described by the following expression:

$$H'_a = H'^0_a - kx^{1/3} \quad (7)$$

with H'^0_a being the association enthalpy at infinite dilution, k a constant, and x (in $Ce_{1-x}RE_xO_{2-x/2}$) the doping ion content.

Within this framework, the observed decrease in H'_a occurring with increasing the doping ion content is mediated by the term $kx^{1/3}$, which represents the interaction energy between oxygen vacancies and the charges distributed within the lattice due to the presence of charged dimers. In other words, the dimers association enthalpy decreases with increasing the RE^{3+} concentration (and hence the dimers concentration), due to the interaction between vacancies and the electrostatic field generated by charged dimers, which reduces the energy needed to separate a vacancy from its RE counterpart. If applied to data of $Ce_{1-x}(Nd_{0.74}Tm_{0.26})_xO_{2-x/2}$, eq. (7) provides the trend shown in the inset to Fig. 13: data are excellently fitted by a regression line (r^2 = 0.988), thus confirming that the trend observed in Y-doped ceria [61] is also followed by the present system. Lastly, it is also noteworthy that the value of H'_a extrapolated at x = 0, namely H'^0_a, is around 1.2 eV, in good agreement with the binding energies expected close to zero strain for $1V_O^{\bullet\bullet}Y'_{Ce}$ and $1V_O^{\bullet\bullet}Gd'_{Ce}$ dimers [63], *i.e.* for defect associates containing trivalent ions close in size to Tm^{3+} and Nd^{3+} ($r_{Tm3+,CN8}$ = 0.994 Å, $r_{Nd3+,CN8}$ = 1.109 Å, $r_{Y3+,CN8}$ = 1.019 Å, $r_{Gd3+,CN8}$ = 1.053 Å) [34]. This evidence strengthens the hypothesis that the apparent association enthalpy, namely $E_a(LT) - E_a(HT)$, indeed corresponds to the $1V_O^{\bullet\bullet}2RE'_{Ce}$ trimers association enthalpy.

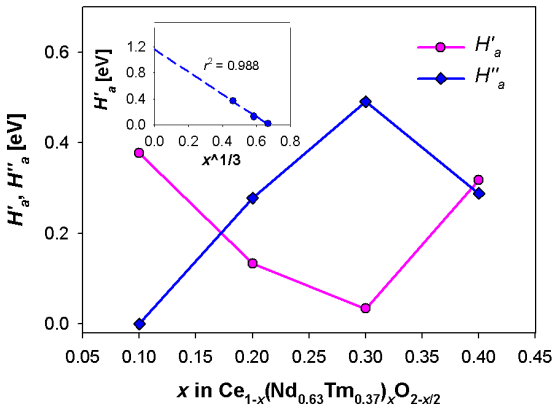

Fig. 13. H'_a and H''_a calculated according to eqs. (5) and (6) as a function of *x*. Data are connected by broken lines. Inset: plot of H'_a *vs. x*^1/3. The dashed line is the regression line fitting data, described by the equation H'_a = -1.7244 $x^{1/3}$ + 1.1610, with r^2 = 0.988.

It can be concluded that the main advantage brought about by co-doping resides in the separation of a high and a low temperature conduction behaviour, allowing the attainment of activation energies in the high temperature regime lower than the ones of singly doped systems. The literature offers a wide variety of studies on RE-doped ceria systems either presenting [2,10,64] or not [3,52] the two different conduction regimes; nevertheless, the double activation energy is almost always reported for multiply doped ceria, such as (La,Dy)- [16], (La,Sm)- [10], (La,Fe)- [10], (Sm,Fe)- [10], (Gd,Nd)- [5,9], (Sm,Gd)- [9], (Sm,Nd)- [9], (Sm,Gd,Nd)- [9] based systems. This evidence is attributable to the large difference in binding energy between defect aggregates containing RE^{3+} ions different in size: the smaller RE^{3+} ions are mainly trapped into trimers, which with increasing temperature dissociate due to their low configurational entropy, while dimers survive, making clearly detectable the slope change in the Arrhenius plot. Within this scenario, the CeO_2 solid solution is expected to host predominantly RE'_{Ce} isolated defects with RE coinciding with the larger ion, as confirmed by results of the crystallographic and spectroscopic analyses performed on $Ce_{1-x}(Nd_{0.74}Tm_{0.26})_xO_{2-x/2}$. Moreover, thanks to the occurrence of two well distinguishable activation energies, $E_a(HT)$ is significantly lower than E_a of both Sm- and Nd-doped ceria: at *x* = 0.2, for example, $E_a(HT)$ is around 0.7 eV for (Nd,Tm)-doped ceria, while E_a ~0.8 eV and 1.19 eV for Sm- [52] and Nd- [3] doped ceria, respectively. As a corollary of this discussion on doubly-doped ceria systems, it is questionable whether a similar scenario in terms of structural and transport properties also appears when it comes to tri- and more generally to multiply-doped

systems: even if not numerous, studies on tri-doped ceria generally point at a larger compositional F stability region than in singly-doped ceria, such as in the case of $Ce_{1-x}(Pr_{1/3}Gd_{1/3}Sm_{1/3})_xO_{2-x/2}$ [65], so that it is reasonable to hypothesize that a similar mechanism as in doubly-doped ceria takes place, with smaller ions entering C clusters and larger ones being preferably located within F.

5. Conclusions

The correlations between structural and transport properties of $Ce_{1-x}(Nd_{0.74}Tm_{0.26})_xO_{2-x/2}$ ($0.1 \leq x \leq 0.6$) were investigated. The system was chosen as the average size of the doping ions mixture corresponds to that of Sm^{3+}, namely one of the most effective dopants for ceria-based systems in terms of ionic conductivity.

The main experimental results can be summarized as follows: a) if compared to Sm-doped ceria, at each x value cell parameters are larger and the compositional extent of the CeO_2-based solid solution is wider; b) two different values of activation energy to ionic conduction occur within different temperature ranges, with the low/high temperature crossover being located at ~750 K.

These evidences agree with the prevailing formation of $1V_O^{\bullet\bullet}2Tm'_{Ce}$ trimers, and with their dissociation at high temperature. The occurrence of these defect aggregates favours the entrance of Nd'_{Ce} isolated defects into the CeO_2-based solid solution, thus causing the enlargement of its stability region and an increase of cell parameters. Moreover, the hypothesized disappearance of trimers in the high temperature range provides a value of the $1V_O^{\bullet\bullet}RE'_{Ce}$ dimers binding energy in very good accordance with results of simulations.

Acknowledgements

Authors would like to acknowledge the Elettra synchrotron facility for the provision of beamtime. This work was financially supported by Compagnia di San Paolo, in the frame of the project COLEUS – ID ROL: 32604.

References

[1] C. Artini, Inorg. Chem. 57 (2018) 13047-13062.
[2] S. Omar, E.D. Wachsman, J.L. Jones, J.C. Nino, J. Am. Ceram. Soc. 92 (2009) 2674-2681.
[3] K.A. Bhabu, J. Theertagiri, J. Madhavan, T. Balu, T.R. Rajasekaran, J. Phys. Chem. C 120 (2016) 18452-18461.
[4] C. Artini, L. Gigli, M.M. Carnasciali, M. Pani, Inorganics 7 (2019) 94.
[5] A. Arabaci, T.G. Altınçekiç, M. Der, M.A.F. Öksüzömer, J. Alloy Compd. 792 (2019) 1141-1149.
[6] F.-Y. Wang, S. Chen, S. Cheng, Electrochem. Commun. 6 (2004) 743-746.
[7] W. Zayąc, J. Molenda, Solid State Ionics 179 (2008) 154-158.
[8] N. Kim, B.H. Kim, D. Lee, J. Power Sources 90 (2000) 139-143.
[9] A.V. Coles-Aldridge, R.T. Baker, Solid State Ionics 316 (2018) 9-19.
[10] M. Gupta, S. Shirbhate, P. Ojha, S. Acharya, Solid State Ionics 320 (2018) 199-209.
[11] S. Omar, E. Wachsman, J. Nino, Solid State Ionics 178 (2008) 1890-1897.
[12] A.S. Babu, R. Bauri, ECS Trans. 57 (2013) 1115-1123.
[13] G. Accardo, G. Dell'Agli, L. Spiridigliozzi, S.P. Yoon, D. Frattini, Int. J. Hydrog. Energy 2020, DOI: 10.1016/j.ijhydene.2020.05.011.
[14] A. Arabaci, V. Sariboğa, M.A.F. Őksüzőmer, Metall. Mater. Trans. A 45 (2014) 5259-5269.
[15] C. Madhuri, K. Venkataramana, A. Nurhayati, C. Vishnuvardhan Reddy, Curr. Appl. Phys. 18 (2018) 1134-1142.
[16] K. Venkataramana, C. Madhuri, C. Madhusudan, Y. Suresh Reddy, G. Bhikshamaiah, C. Vishnuvardhan Reddy, Ceram. Int. 44 (2018) 6300-6310.
[17] S. Omar, in: S.B. Khan, K. Akhtar, (Eds.), *Cerium oxide – Applications and attributes*, IntechOpen, London, 2019, Chapter 4.
[18] M. Mogensen, N.M. Sammes, G.A. Tompsett, Solid State Ionics 129 (2000) 63–94.
[19] M. Coduri, S. Checchia, M. Longhi, D. Ceresoli, M. Scavini, Front. Chem. 6 (2018) 526.
[20] L. Eyring, in: K.A. Gschneidner Jr, L. Eyring (Eds.), Handbook on the Physics and Chemistry of Rare Earths, North Holland, Amsterdam, 1979, Chapter 3, pp. 337-399.
[21] Z.P. Li, T. Mori, J. Zou, J. Drennan, Mater. Res. Bull. 48 (2013) 807-812.
[22] B. Wang, R.J. Lewis, A.N. Cormack, Acta Mater. 59 (2011) 2035-2045.
[23] G. A. Costa, C. Artini, A. Ubaldini, M.M. Carnasciali, P. Mele, R. Masini, J. Therm. Anal. Calorim. 92 (2008) 101-104.
[24] C. Artini, M. M. Carnasciali, G. A. Costa, J. R. Plaisier, M. Pani, Solid State Ionics 311 (2017) 90-97.
[25] C. Artini, M. Pani, M.M. Carnasciali, J. R. Plaisier, G. A. Costa, Inorg. Chem. 55 (2016) 10567-10579
[26] M. Coduri, M. Scavini, M. Pani, M. M. Carnasciali, H. Klein, C. Artini, Phys. Chem. Chem. Phys. 19 (2017) 11612-11630.
[27] C. Artini, G.A. Costa, M. Pani, A. Lausi, J. Plaisier, J. Solid State Chem. 190 (2012) 24-28.
[28] L. Minervini, M.O. Zacate, R.W. Grimes, Solid State Ionics 116 (1999) 339-349.
[29] F. Ye, T. Mori, D. Ou, A.N. Cormack, Solid State Ionics 180 (2009) 1127-1132.
[30] D.R. Ou, F. Ye, T. Mori, Phys. Chem. Chem. Phys. 13 (2011) 9554-9560.
[31] H. Yamamura, E. Katoh, M. Ichikawa, K. Kakinuma, T. Mori, H. Haneda, Electrochem. 68 (2000) 455-459.
[32] J. Van Herle, D. Seneviratne, A.J. Mc Evoy, J. Eur. Ceram. Soc. 19 (1999) 837-841.

[33] C. Artini, M. Pani, M.M. Carnasciali, M.T. Buscaglia, J. Plaisier, G.A. Costa, Inorg. Chem. 54 (2015) 4126-4137.
[34] R.D. Shannon, Acta Crystallogr. A32 (1976) 751-767.
[35] C. Artini, G.A. Costa, R. Masini, J. Therm. Anal. Calorim. 103 (2011) 17-21.
[36] J.R. Plaisier, L. Nodari, L. Gigli, E.P.R.S. Miguel, R. Bertoncello, A. Lausi, Acta Imeko 6 (2017) 71-75.
[37] P. Thompson, D.E. Cox, J.B. Hastings, J. Appl. Cryst. 20 (1987) 79-83.
[38] J Rodriguez-Carvajal, Phys. B: Condensed Matter 192 (1993) 55-69.
[39] L. Vegard, H. Dale, Zeitschr. Krist. 67 (1928) 148-162.
[40] C. Artini, M. Pani, A. Lausi, R. Masini, G.A. Costa, Inorg. Chem. 53 (2014) 10140-10149.
[41] G.K. Williamson, W.H. Hall, Acta Metall. 1 (1953) 22-31.
[42] W.H. Weber, K.C. Hass, J.R. Mc Bride, Phys. Rev. B 48 (1993) 178-185.
[43] J.R. Mc Bride, K.C. Hass, B.D. Poindexter, W.H. Weber, J. Appl. Phys. 76 (1994) 2435-2441.
[44] A. Ubaldini, M.M. Carnasciali, J. Alloy Compd. 454 (2008) 374-378.
[45] A. Kossoy, Q. Wang, R. Korobko, V. Grover, Y. Feldman, E. Wachtel, A.K. Tyagi, A.I. Frenkel, I. Lubomirsky, Phys. Rev. B 87 (2013) 054101.
[46] B.P. Mandal, V. Grover, M. Roy, A.K. Tyagi, J. Am. Ceram. Soc. 90 (2007) 2961-2965.
[47] D. Marrocchelli, S.R. Bishop, H.L. Tuller, G.W. Watson, B. Yildiz, Phys. Chem. Chem. Phys. 14 (2012) 12070-12074.
[48] M. Coduri, M. Scavini, M. Allieta, M. Brunelli, C. Ferrero, Chem. Mater. 25 (2013) 4278-4289.
[49] M.B. Isichenko, Rev. Mod. Phys. 64 (1992) 961-1043.
[50] A. Nakajima, A. Yoshihara, M. Ishigame, Phys. Rev. B 50 (1994) 13297-13307.
[51] C. Artini, M. M. Carnasciali, M. Viviani, S. Presto, J. R. Plaisier, G. A. Costa, M. Pani, Solid State Ionics 315 (2018) 85-91.
[52] S. Presto, C. Artini, M. Pani, M.M. Carnasciali, S. Massardo, M. Viviani, Phys. Chem. Chem. Phys. 20 (2018) 28338-28345.
[53] B.C.H. Steele, Solid State Ionics 129 (2000) 95-110.
[54] J. Koettgen, S. Grieshammer, P. Hein, B.O.H. Grope, M. Nakayama, M. Martin, Phys. Chem. Chem. Phys. 20 (2018) 14291-14321.
[55] R. Schmitt, A. Nenning, O. Kraynis, R. Korobko, A.I. Frenkel, I. Lubomirsky, S.M. Haile, J.L.M. Rupp, Chem. Soc. Rev. 49 (2020) 554-592.
[56] K. Muthukkumaran, R. Bokalawela, T. Mathews, S. Selladurai, J. Mater. Sci. 42 (2007) 7461-7466.
[57] S.V. Chavan, M.D. Mathews, A.K. Tyagi, Mater. Res. Bull. 40 (2005) 1558-1568.
[58] S.V. Chavan, A.K. Tyagi, Mater. Sci. Eng. A 404 (2005) 57-63.
[59] D. Horlait, L. Claparède, N. Clavier, S. Szencnekt, N. Dacheux, J. Ravaux, R. Podor, Inorg. Chem. 50 (2011) 150-161.
[60] H. Inaba, H. Tagawa, Solid State Ionics 83 (1996) 1-16.
[61] D. Wang, D.S. Park, J. Griffith, A.S. Nowick, Solid State Ionics 2 (1981) 95–105.
[62] J. Faber, C. Geoffroy, A. Roux, A. Sylvestre, P. Abélard, Appl. Phys. A 49 (1989) 225-232.
[63] M.J.D. Rushton, A. Chroneos, S.J. Skinner, J.A. Kilner, R.W. Grimes, Solid State Ionics 230 (2013) 37-42.
[64] C. Artini, S. Presto, S. Massardo, M. Pani, M.M. Carnasciali, M. Viviani, Energies 12 (2019) 4148.
[65] K. Venkataramana, C. Madhuri, Y. Suresh Reddy, G. Bhikshamaiah, C. Vishnuvardhan Reddy, J. Alloy Compd. 719 (2017) 97-107.

Graphical Abstract

Description

Evidence for two distinct conduction regimes comes from experimental investigations on co-doped $Ce_{1-x}(Nd_{0.74}Tm_{0.26})_xO_{2-x/2}$ ($0.1 \leq x \leq 0.6$) system. At low temperature defects mainly associate as $1V_O^{\bullet\bullet}2Tm'_{Ce}$, trimers, which dissociate above 750 K inducing a lower activation energy.

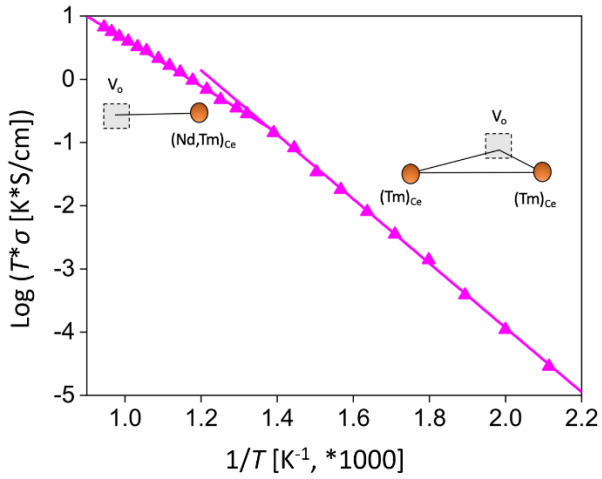

Declaration of interests

☒ The authors declare that they have no known competing financial interests or personal relationships that could have appeared to influence the work reported in this paper.

☐The authors declare the following financial interests/personal relationships which may be considered as potential competing interests:

- The co-doped ceria system $Ce_{1-x}(Nd_{0.74}Tm_{0.26})_xO_{2-x/2}$ ($x \leq 0.6$) has been investigated.
- Structural and microstructural features of the material have been emphasized.
- Ionic conductivity was studied by impedance spectroscopy.
- Two different activation energies are clearly visible from the Arrhenius plot.
- The pattern of defects aggregation agrees with structural and transport properties.